Geophys. J. Int. (2003) **153,** 344–358

Elastic wave propagation in anisotropic crustal material possessing arbitrary internal tilt

David A. Okaya[1] and Thomas V. McEvilly[2]

[1]*Department Earth Sciences, University of Southern California, Los Angeles,* CA 90089-0740*, USA. E-mail: okaya@usc.edu*
[2]*Department Geology and Geophysics, University of California, Berkeley,* CA 94720*, USA*

Accepted 2002 October 10. Received 2002 October 3; in original form 2002 March 7

SUMMARY

Geological causes of crustal anisotropy include regional fractures and cracks, isotropic heterogeneity or layering and material composition and textural properties. In addition, shear or metamorphic foliations in fault zones or structural terranes can serve as proxies for intracrustal deformation in a manner analogous to the lattice-preferred orientation of olivine produced by mantle shear. The primary factor in the production of crustal anisotropy is the relative angle between a seismic wave and the (dipping) symmetry axes of crustal material as either change along the propagation ray path. Complex and heterogeneous, crustal material is not necessarily oriented with vertical/horizontal symmetry axes, but is more normally tilted in accordance with structure. Calculation of the anisotropic response to material tilt for elastic seismic wave propagation requires rotation of the stiffness tensors describing the crustal material. We examine the alteration of anisotropic stiffness tensors and provide rotation directional cosines based on geological measurements. Material tilt produces strong effects in examples of 2-D and 3-D finite-difference synthetic seismograms that might otherwise be attributed to velocities or structure in other regions of the crust or mantle.

Key words: elastic-wave theory, finite-difference methods, seismic anisotropy, seismic modelling, seismic wave propagation.

INTRODUCTION: WAVE PROPAGATION IN HETEROGENEOUS ANISOTROPIC CRUSTAL MEDIA

While recent studies have examined the effect of lattice-preferred orientation of olivine-rich rocks in the mantle (e.g. Savage *et al.* 1990; Silver & Chan 1991; Russo & Silver 1994; Savage 1999), fewer studies have investigated the role of inherent material anisotropy on seismic propagation within the crystalline crust. These latter studies are made more complex because of the presence in the crust of geological heterogeneity and changing ray path orientations caused by strong seismic velocity gradients. Whether the raypaths or structure change orientation in these situations, the waveform effects of particle motion, traveltime delays and shear wave splitting are a result of the same cause: the relative angle of the incoming propagating wave with respect to the orientation of the material anisotropy. Christoffel velocity equations for anisotropic media (e.g. Hearmon 1961) indicate that large variation in *P*- and *S*-wave velocities can occur as functions of this relative angle (Fig. 1). As a result, calculations of anisotropic effects are not simple in areas of complex crystalline crust and in some cases may only be solved numerically. Calculation of synthetic seismograms using finite-difference methods allows for full 3-D variability in severity and orientation (tilt) of anisotropic material symmetries plus in composition, large-scale features and internal structures.

Material anisotropy may be produced in crystalline crustal rocks by composition, layering or deformational/metamorphic textures such as schistocity or gneissic fabrics. These textures may be localized within shear zones and deformational fronts or may be penetrative to form extensive subsurface regions of foliated rock such as the Haast schist terrane in New Zealand (Okaya *et al.* 1995). For these schists, their foliation represents a planar arrangement of (micaceous) minerals. An associated lineation if present is the preferred linear alignment of the minerals or striations that often indicates the dominant tectonic transport or shear direction. Brocher & Christensen (1990) observed different refraction P_g velocities in orthogonal directions within the foliated Chugach schist terrane in southern Alaska. Tectonically aligned orientation of similar or disparate rocks produce bulk anisotropy in the extensional ductile lower crust of the Basin and Range Province, which is observed as differing Moho reflection two-way traveltimes in perpendicular profiles (Carbonell & Smithson 1991) and in P_s converted phases (McNamara & Owens 1993). Pronounced shear wave splitting occurs in vertical seismic profile data collected at the 9 km KTB drillhole in the central European Variscan belt as a result of the presence of strongly foliated amphibolites and gneisses (Rabbel & Luschen 1996). Petrophysical measurements indicate that up to 15–20 per cent velocity anisotropy can be produced by these metamorphic and

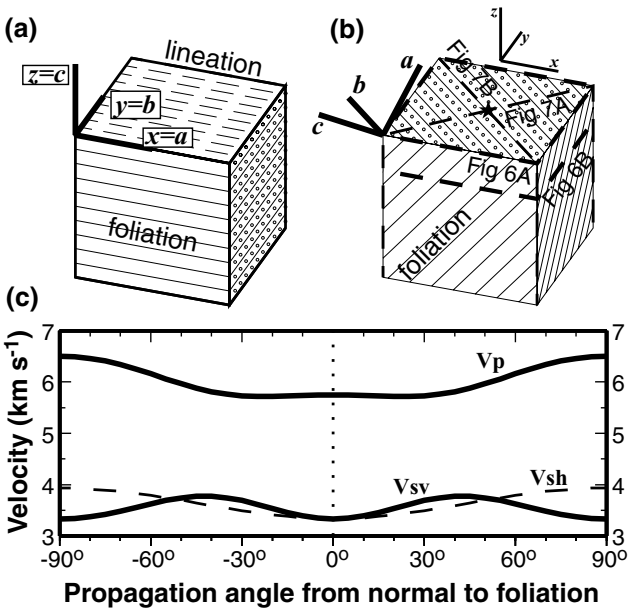

Figure 1. Seismic waves propagate in different directions through an anisotropic material. (a) Block of foliated rock with no tilt; material *a–b–c* axes are coincident with geographical *x–y–z* axes. In this orientation the fast *P* velocity is aligned with lineation (*a*-axis), whereas the slowest *P* velocity is normal to foliation (*c*-axis). Shear particle motion is fastest within the *a–b* plane and slower in all other directions. For transverse isotropy (hexagonal symmetry) the *a* and *b* directions have the same behaviour. (b) Block with foliation dips at 60° and strikes 135° counter-clockwise from the *x*-axis. Note the tilted *a–b–c* axes with respect to *x–y–z*. The bold dashed lines indicate horizontal planes through which propagating waves are shown in Fig. 6 while thin dashed lines indicate vertical diagonal slices shown in Fig. 7; a star denotes the source point used in both figures. (c) *P* and *SV/SH* velocities as a function of the propagation angle as measured from the normal to foliation (*c*-axis in a hexagonal symmetry). These velocity curves were calculated from hexagonal Christoffel equations (Hearmon 1961) using Haast schist velocities. Large angular variations in all three velocities indicate possible complexities in wave propagation behaviour when the wave-material axes angle varies.

tectonic foliations (Fountain & Christensen 1989; Godfrey *et al.* 2000). Jones *et al.* (1996) and Godfrey *et al.* (2002) examine the effects of propagation traveltime delays owing to crustal anisotropy when using isotropic-velocity algorithms for the analyses of active-source seismic data.

A full solution of anisotropic wave propagation will account for heterogeneities in material properties (e.g. velocities and densities), the degree of anisotropy (isotropy versus differing symmetries of anisotropy), and the orientation of the anisotropy (not necessarily aligned to horizontal/vertical or to layer boundaries). Prior studies of anisotropic wave propagation account for heterogeneity in some but not all of these material traits. Studies exist that use transversely isotropic material that have boundary dip but with untilted internal fabric (Tsingas *et al.* 1990; Faria & Stoffa 1994a; Savage 1998) or have a uniformly tilted internal fabric, but horizontal to constant dipping boundaries (Alkhalifah 1995; Levin & Park 1997, who review several papers in which tilted anisotropic material may affect the observed propagation effects; Frederiksen & Bostock 2000). Propagation in untilted material is described by analytical solutions (Mensch & Rasolofosaon 1997) and by numerical solutions (Keith & Crampin 1977; Payton 1983; Carcione 1990; Faria & Stoffa 1994a; Girardin & Farra 1998; Hung & Forsyth 1998). Traveltime (non-waveform) solutions are provided by Faria & Stoffa (1994b) and Grechka & McMechan (1997), who allow for dipping layers but untilted material; similarly, ray-tracing methods for seismograms are described by Daley & Hron (1979), Cerveny & Firbas (1984), Gajewski & Pscencik (1987) and Grechka & McMechan (1996). A spectral method for general material anisotropy is described by Tessmer (1995). Finite-difference methods that can allow for the greatest amount of heterogeneities are used for the 2-D transverse isotropy case by Tsingas *et al.* (1990), Faria & Stoffa (1994a) and by Juhlin (1995) who provides a description of arbitrary tilt in 2-D for *P–SV* seismograms. Igel *et al.* (1993) discuss issues associated with 3-D finite-difference implementation. Zhu & Dorman (2000) use finite elements to compute in 2-D arbitrary tilt for three-component seismograms. In this study we examine material anisotropy for arbitrarily oriented crustal material in order to compute in 3-D three-component anisotropic elastic wavefield seismograms using finite differences.

ELASTIC WAVE PROPAGATION IN TILTED ANISOTROPIC MEDIA

The full anisotropic elastic wave equation can be expressed as $\rho d^2u_i/dt^2 = c_{ijkl}d^2u_k/dx_l dx_j$, where ρ denotes density, u denotes displacement (as a function of position x, y, z and time t) and c_{ijkl} is the elastic stiffness tensor. Symmetries that are available to define the stiffness tensors for crystalline crustal rocks are summarized in Fig. 2. The higher 'ordered' orthorhombic, hexagonal, cubic and isotropic symmetries have the same stiffness pattern but differ in the number of interrelated terms. To propagate waves within an anisotropic material possessing internal tilt, the stiffness tensor within the elastic wave equation needs to be oriented via tensor rotation (Sands 1982; Nye 1985). The anisotropic form

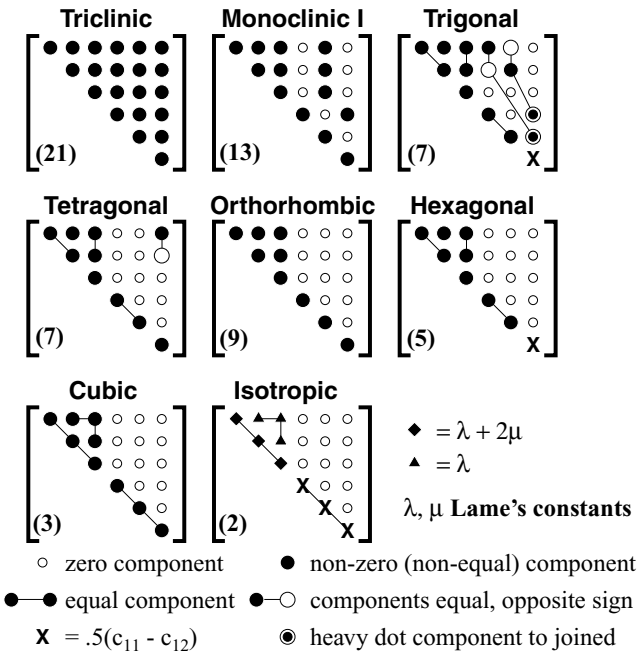

Figure 2. Patterns of stiffness tensors for crystal and material symmetries (adapted from Nye 1985). The tensor patterns are in reduced matrix notation and are symmetric about the diagonal, hence only the upper right-hand side of each matrix is shown for clarity. Triclinic symmetry requires all 21 coefficients, whereas hexagonal symmetry requires five independent terms to define its nine non-zero elements.

of stress–strain elasticity is thus $\boldsymbol{\sigma} = \{\mathbf{McM}^{\mathrm{T}}\}\varepsilon$ and when written in reduced matrix notation is

$$\begin{vmatrix}\sigma_1\\ \sigma_2\\ \sigma_3\\ \tau_4\\ \tau_5\\ \tau_6\end{vmatrix} = \mathbf{M} \begin{vmatrix} c_{11} & c_{12} & c_{13} & c_{14} & c_{15} & c_{16}\\ & c_{22} & c_{23} & c_{24} & c_{25} & c_{26}\\ & & c_{33} & c_{34} & c_{35} & c_{36}\\ & \text{(diagonal} & & c_{44} & c_{45} & c_{46}\\ & \text{symmetry)} & & & c_{55} & c_{56}\\ & & & & & c_{66}\end{vmatrix} \mathbf{M}^{\mathrm{T}} * \begin{vmatrix}\varepsilon_1\\ \varepsilon_2\\ \varepsilon_3\\ \varepsilon_4\\ \varepsilon_5\\ \varepsilon_6\end{vmatrix}, \tag{1}$$

where σ and τ are normal and shear stresses, ε is strain, $\mathbf{M}$ and $\mathbf{M}^{\mathrm{T}}$ are the tensor rotation operator and its transpose, and the reduced subscripts are $1 = xx$, $2 = yy$, $3 = zz$, $4 = yz$, $5 = xz$ and $6 = xy$ (Auld 1973; Nye 1985). To allow for heterogeneous geological dips and internal foliation fabrics, each internal grid point within the finite-difference implementation requires its own stiffness tensor, which may be rotated by its own degree of tilt. Fortunately, these tensor manipulations are simplified in reduced matrix notation to a matrix rotation as discussed below.

As a matter of convention the symmetry axes of a foliated material is defined here as follows. The *a*–*b* axes are in the foliation plane so that *a* is associated with exhibited lineation; as a result the *c*-axis is normal to foliation (Fig. 1). In terms of seismic velocities the fastest V_P direction is thus parallel to the *a*-axis and the slowest V_P is parallel to the *c*-axis. When not tilted, by convention the symmetry axes *a*, *b* and *c* are aligned with the geographical *x*, *y* and *z* axes, respectively (Fig. 1a). In this definition untilted foliation planes lie horizontal and the *a*–*b* axes are interchangeable for hexagonal symmetry. When tilted, the *a*–*b*–*c* axes separate from the *x*–*y*–*z* axes by an amount specified by the directional cosines.

Stiffness tensors of crustal crystalline rocks

Strongly foliated rocks such as gneisses and schists are orthorhombic or lower in symmetry. However, compilations of laboratory measurements of many laminated or foliated rocks by Christensen (1965, 1966), Fountain & Christensen (1989) and Godfrey *et al.* (2000) reveal that orthogonal measurements within the planes of foliation are similar (less than a few per cent) particularly when compared with the measurement normal to the planes (several to >10 per cent). In these cases the approximation of hexagonal symmetry is valid. Additional anisotropic materials such as shales, bedded strata or regularly cracked media are often strongly laminated or foliated; most seismic studies also define these materials as hexagonal (Thomsen 1986; Cristescu 1989; Helbig 1993). The stiffness elements of this symmetry are calculated from five independent *P*- and *S*-wave velocities as measured in the laboratory or in the field (Christensen & Crosson 1968; Cristescu 1989). Measurements diagonal (45°) to the principal symmetry axes are required for any symmetry that has more than three independent elements (Nye 1985; Thomsen 1986); the single diagonal measurement for hexagonal symmetry profoundly influences shear wave splitting behaviour (Okaya & Christensen 2002). These diagonal measurements are relatively difficult to perform and have seldom been made, making a full definition of tetragonal or

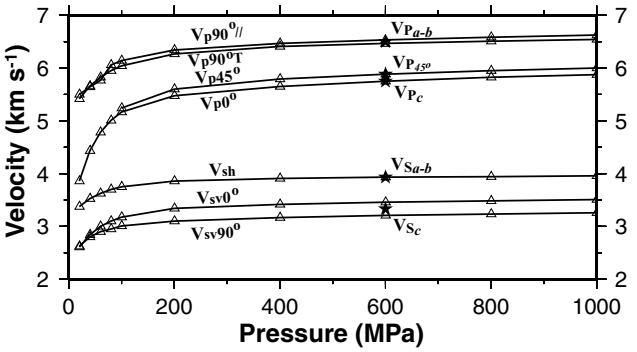

Figure 3. Velocity–pressure curves for the Haast schist, New Zealand. Petrophysical measurements were conducted along principal axes (e.g. Fig. 1a) and one diagonal direction at confining pressures of up to 1000 MPa. Degrees indicate orientation of wave relative to *c*-symmetry axis. $V_{P90^\circ\parallel}$ and $V_{P90^\circ\mathrm{T}}$ are both in the plane of foliation and either parallel or perpendicular to lineation, respectively, and are nearly identical. V_{SH} is propagation and particle motion within the plane of foliation. V_{SV0° propagates parallel to the symmetry axis with particle motion in the plane of foliation; V_{SV90° is within the plane of foliation with particle motion parallel to the symmetry axis. These V_{SV} are similar. A hexagonal symmetry can be used to approximate this orthorhombic schist (stars). Velocities at 600 MPa are used in the calculations of synthetic seismograms shown in subsequent figures.

$$[\mathbf{M}] = \left|\begin{array}{ccc|ccc} \alpha^2_{ax} & \alpha^2_{ay} & \alpha^2_{az} & 2\alpha_{ay}\alpha_{az} & 2\alpha_{az}\alpha_{ax} & 2\alpha_{ax}\alpha_{ay} \\ \alpha^2_{bx} & \alpha^2_{by} & \alpha^2_{bz} & 2\alpha_{by}\alpha_{bz} & 2\alpha_{bz}\alpha_{bx} & 2\alpha_{bx}\alpha_{by} \\ \alpha^2_{ax} & \alpha^2_{cy} & \alpha^2_{cz} & 2\alpha_{cy}\alpha_{cz} & 2\alpha_{cz}\alpha_{cx} & 2\alpha_{cx}\alpha_{cy} \\ \hline \alpha_{bx}\alpha_{cx} & \alpha_{by}\alpha_{cy} & \alpha_{bz}\alpha_{cz} & \alpha_{by}\alpha_{cz}+\alpha_{bz}\alpha_{cy} & \alpha_{bx}\alpha_{cz}+\alpha_{bz}\alpha_{cx} & \alpha_{by}\alpha_{cx}+\alpha_{bx}\alpha_{cy} \\ \alpha_{cx}\alpha_{ax} & \alpha_{cy}\alpha_{ay} & \alpha_{cz}\alpha_{az} & \alpha_{ay}\alpha_{cz}+\alpha_{az}\alpha_{cy} & \alpha_{az}\alpha_{cx}+\alpha_{ax}\alpha_{cz} & \alpha_{ax}\alpha_{cy}+\alpha_{ay}\alpha_{cx} \\ \alpha_{ax}\alpha_{bx} & \alpha_{ay}\alpha_{by} & \alpha_{az}\alpha_{bz} & \alpha_{ay}\alpha_{bz}+\alpha_{az}\alpha_{by} & \alpha_{az}\alpha_{bx}+\alpha_{ax}\alpha_{bz} & \alpha_{ax}\alpha_{by}+\alpha_{ay}\alpha_{bx} \end{array}\right|$$

Figure 4. Bond transformation matrix in reduced matrix notation (Auld 1973). This operator is equivalent to a tensor rotation. Element α_{ij} is the directional cosine between a tilted symmetry axis $i = a, b, c$ and a geographical axis $j = x, y, z$.

orthorhombic anisotropic behaviour rare (e.g. Christensen & Ramananantoandro 1971). The lower-ordered symmetries (triclinic, monoclinic and trigonal) are even more rarely used as materials within studies of crustal wave propagation owing to the number of measurements required (Fig. 2).

We illustrate an example of a stiffness tensor for crystalline crust that we will use in subsequent synthetic modelling. Davey *et al.* (1997) identify a major schist terrane in the central South Island, New Zealand that is subhorizontal underneath a significant portion of the island but is tectonically upturned to a near-vertical orientation at the adjacent Pacific/Indo-Australian plate boundary. Velocity–pressure curves were obtained from samples of this 'Haast' schist for *P*- and *S*-wave propagation along the principal symmetry axes (Okaya *et al.* 1995; Godfrey *et al.* 2000). These curves indicate up to 17 per cent *P*-wave and 18 per cent *S*-wave anisotropy (Fig. 3). Very similar are V_P along the *a* and *b* axes ($V_{P90^\circ\parallel}$ and $V_{P90^\circ\mathrm{T}}$, respectively) and V_{SV} normal and in the plane of foliation (V_{SV0° and V_{SV90°, respectively). Thus, we may define a hexagonal stiffness tensor for this schist. At 600 MPa, which approximates mid-crustal levels, the Haast schist velocities are: $V_{Pab} = 6501$ m s^{-1}, $V_{Pc} = 5750$ m s^{-1}, $V_{P45^\circ} = 5881$ms^{-1}, $V_{\mathrm{Sab}} = 3931$ m s^{-1} (propagation and particle motion in the foliation planes), $V_{Sc} = 3332$ m s^{-1} (propagation or particle motion normal to foliation and thus parallel to the *c*-axis), and density $= 2718$ kg m^{-3}. The unrotated stiffness coefficients (in GPa) are thus $c_{11} = c_{22} = 114.87$, $c_{33} = 89.86$, $c_{44} = c_{55} = 30.18$, $c_{66} = 42.00$, $c_{12} = 30.87$ and $c_{13} = c_{23} = 23.86$. Velocity variation owing to the incoming propagation direction can be calculated using these stiffness values in the Christoffel equations (Hearmon 1961). Fig. 1(c) reveals that V_P, V_{SV} and V_{SH} are all relatively slower when nearly normal to foliation (*c*-direction). V_P and V_{SH} are fast in the foliation planes while V_{SV} reaches a maximum at approximately 40°. V_P and V_{SH}–V_{SV} splitting behaviour varies widely in directions between the *c*- and *a*–*b* axes, indicating possible complexities when seismic waves propagate through heterogeneous structure.

Modification of the stiffness tensor by tilt

The effect of tilt on a material can be thought of as decreasing the symmetrical 'order' of the material. This can be illustrated by examining a material of hexagonal symmetry prior to and after stiffness rotation. This rotation is a matrix operation in reduced matrix notation using the Bond transformation operator (Fig. 4), which uses directional cosines to relate the desired orientation to the unrotated coordinate frame (Auld 1973; Jaeger & Cook 1976). In Fig. 5 an unrotated hexagonal symmetry is displayed where the magnitudes of the stiffness coefficients are represented only as zero or filled values. The matrix is symmetrical about the diagonal so that for simplicity only the upper right-hand face is displayed and discussed here. For this symmetry there are nine filled elements of which four are related to the other five (Fig. 2). A rotation about the *x*-axis leaves only the coefficient c_{11} unchanged. The other eight original coefficients are modified and those that had been equal are not necessarily equal after rotation. In addition, four new coefficients appear, which were originally zero-valued (Fig. 5). A similar modification occurs if the original hexagonal symmetry is rotated about the *y*- or *z*-axis. Juhlin (1995) uses the *x*–*z* components of a rotation

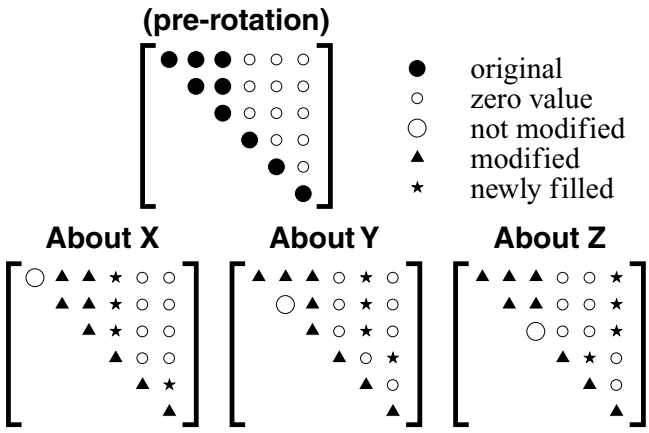

Figure 5. Effect of rotation on hexagonal symmetry. The pre-rotation pattern of stiffness elements are shown above the modification to the elements upon rotation about each principal axis. The reduced notation matrices are symmetric about the diagonal and hence only the upper right-hand sides are shown. Rotation about a principal axis modifies eight and adds four elements along the diagonal and in the upper right-hand side. This behaviour is also true for orthorhombic symmetry. Rotation about the *Y*-axis yields a pattern similar to monoclinic-I symmetry (Fig. 2), although here the newly filled elements are not independent.

about the *y*-axis to implement *P–SV* finite-difference 2-D modelling; Zhu & Dorman (2000) use the same rotation for 2-D finite-element modelling of three-component seismograms.

A comparison of Figs 2 and 5 reveals that a rotation about the *y*-axis of a hexagonal symmetry produces a pattern similar to monoclinic symmetry, although the number of independent coefficients still remains at five (not 13). An arbitrary tilt angle that is not along any of the principal axes will expand the stiffness matrix so that all 21 elements are filled. As a result, any numerical implementation that calculates anisotropic wave propagation in media with arbitrary tilt must allow for all 21 stiffness coefficients when needed. However, once this full stiffness tensor is implemented, any order of anisotropic symmetry can be used prior to tilting (that is, not limited to transverse isotropy) provided sufficient information such as petrophysical measurements exists in order to realistically define the appropriate values for the stiffness elements.

Directional cosines for tensor rotation

The directional cosines in the rotation tensor of Fig. 4 relate the rotated symmetry axes *a–b–c* to the original geographical axes *x–y–z* and may be defined in several ways. Any definition of directional cosines is acceptable that uses a valid set of measurable reference angles. A description often used in the context of rotations during crystallographic measurements employs Euler angles, which are derived from a sequence of rotations about individual symmetry axes:

$$\alpha_{ij} = \begin{vmatrix} \cos\phi\cos\chi\cos\omega - \sin\phi\sin\omega & \cos\phi\cos\chi\sin\omega + \sin\phi\cos\omega & -\cos\phi\sin\chi \\ -\sin\phi\cos\chi\cos\omega - \cos\phi\sin\omega & -\sin\phi\cos\chi\sin\omega + \cos\phi\cos\omega & \sin\phi\sin\chi \\ \sin\chi\cos\omega & \sin\chi\sin\omega & \cos\chi \end{vmatrix}, \tag{2}$$

where there is first a rotation ω about the *z*-axis, a rotation χ about the modified *y*-axis and then a rotation ϕ about the modified *z*-axis (e.g. Bond 1976; Sands 1982).

The directional cosines may be alternatively expressed in geological measurements of foliation plane strike and dip and lineation trend and plunge:

$$\begin{aligned} \{\alpha_{ax}, \alpha_{ay}, \alpha_{az}\} &= \{\cos t \sin p, \quad \sin t \sin p, \quad \cos p\} \\ \{\alpha_{bx}, \alpha_{by}, \alpha_{bz}\} &= \{\cos s \cos d \cos p - \sin d \sin t \sin p, \quad \sin s \cos d \cos p + \sin d \cos t \sin p, \quad -\cos d \sin p(\sin s \sin t + \cos s \cos t)\} \\ \{\alpha_{cx}, \alpha_{cy}, \alpha_{cz}\} &= \{-\sin s \cos d, \quad \cos s \cos d, \quad \sin d\}, \end{aligned} \tag{3a}$$

where field measurements are first modified so that strike *s* and lineation trend *t* are measured counter-clockwise from due east and the dip *d* and plunge *p* are measured from the vertical (see the derivation in Appendix A). These directional cosines are useful for orienting orthorhombic or lower symmetries. Since the hexagonal symmetry has no lineation and only needs the strike and dip of the foliation plane, the directional cosines reduce to

$$\begin{aligned} \{\alpha_{ax}, \alpha_{ay}, \alpha_{az}\} &= \{\sin s \sin d, -\cos s \sin d, \cos d\} \\ \{\alpha_{bx}, \alpha_{by}, \alpha_{bz}\} &= \{\cos s, \sin s, 0\} \\ \{\alpha_{cx}, \alpha_{cy}, \alpha_{cz}\} &= \{-\sin s \cos d, \cos s \cos d, \sin d\}. \end{aligned} \tag{3b}$$

Finite-difference implementation for waveform synthetics

3-D anisotropic full wavefield propagation can be implemented by inserting the tilted elastic stiffness tensor into the isotropic stress–velocity finite-difference formulation as described by Virieux (1986) and Levander (1988). We modified Graves' (1996) isotropic finite-difference equations of Virieux (fourth order in space and second order in time using staggered grids) so that Lamé constants are replaced by the elastic stiffness tensor. In our implementation, the full 21-element stiffness tensor is defined at each gridpoint when material tilt is present in the earth model. However, when no tilt is requested, for computational efficiency we limit the number of elements to only those needed by the maximum symmetry in the earth model (Fig. 2). The tilted tensor is calculated at each gridpoint only once, prior to the propagation time steps. We also use the A1 absorbing boundary conditions of Clayton & Engquist (1977) and a damping zone on all sides where the width is dependent on the source wavelength. Point and plane wave sources are defined as stress perturbations shaped by a minimum-phase source waveform. For the following examples of anisotropic wave propagation in tilted media, model parametrization and calculation internal time steps were selected to meet stability criteria as summarized by Graves (1996).

ANISOTROPIC PROPAGATION IN UNIFORM FOLIATION FABRIC

In order to observe *P*- and *S*-wave behaviour caused by only tilt (rotation and dip) of an anisotropic material, we propagate an explosive source within a block containing an inclined uniformly foliated material (Fig. 1b). For finite-difference simulation, the earth model is a cube of 2500 m width using 15 m grid spacing. The material foliation is oriented with a northwest–southeast strike and a southwest dip of 60° (Fig. 1b). The stiffness tensor used to define the block material is a hexagonal symmetry using Haast schist velocities at 600 MPa as defined above. A 5–20 Hz explosive source is placed at the centre of the top face and is allowed to propagate into the cube using a time step of 0.001 s for stability. The full three-component stress and velocity fields are calculated at each point in the earth model. This simulation required 1.85 Gbytes of memory and a cumulative 4.53 CPU hours using an eight-node shared-memory SUN Fire 3800 computer with UltraSparc III processors.

The behaviour of the propagating wavefield is revealed when successive time steps are viewed along different slices of the earth model (Fig. 1). Horizontal slices representing the top face and the *x*–*y* plane at 625 m depth are shown in Figs 6(a) and (b), respectively. For both depth slices, the three components of the velocity field are shown at each point with both horizontal components rotated into radial and transverse directions. At 100 and 200 ms in Fig. 6(a), the *P* wave propagates with an elliptical wave front in alignment with the fast and slow directions of the foliation (northwest–southeast strike). Note that since the source is located in this top slice, the *P*-wave compressional motion is essentially radial in direction. A small amount of vertical-component energy in the strike direction suggests the *P*-wave particle motion is responding to the inclined tilt of the rock foliation. The propagating *S* waves appear in the transverse (relative '*SH*') and vertical ('*SV*') planes. Owing to the steep dip, the *S* wave splits when propagating subparallel to the foliation strike (S1 and S2 at 350 ms in Fig. 6a).

Neither the *P* nor *S* wave reach 625 m depth at 100 ms (Fig. 6b). At 200 ms the *P*-wave elliptical wave front is visible but is distorted in the northeast–southwest direction owing to oblique propagation with respect to the tilted material. The S1 and S2 shear waves show coupling

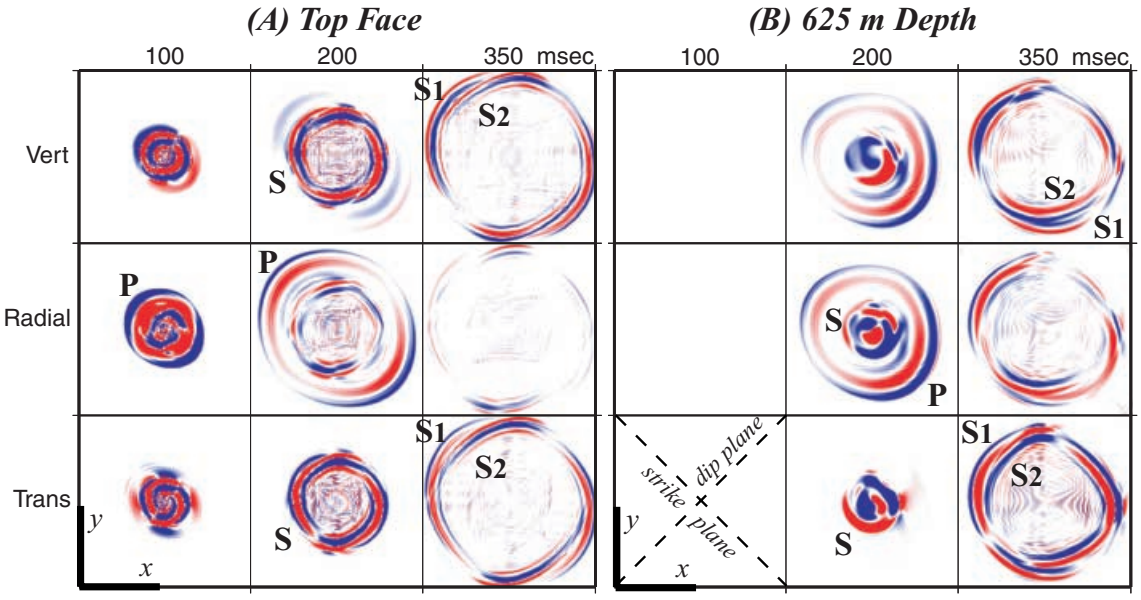

Figure 6. Anisotropic wave propagation in a homogeneous cube that has been rotated so that its foliation strikes N45°W and has *SW* dip of 60° (see Fig. 1b). Cube side is 2500 m using 15 m grid spacing and has Haast schist velocities (Fig. 3). A 5–20 Hz explosive source is at centre of top face. Red is positive seismic amplitude; blue is negative. Three components of motion are shown; the calculated horizontal *x*–*y* components are rotated into radial-transverse directions. Propagation along (a) top face and (b) 1/4 cube length down from top. On the top face *P* wave is elongated in the fast foliation direction (see the radial component at 200 ms). The *S* wave has split in the strike direction. At 625 m depth the *P*- and *S*-wave behaviour become complex owing to dipping foliation plus the oblique downward directions of the propagating wave fronts.

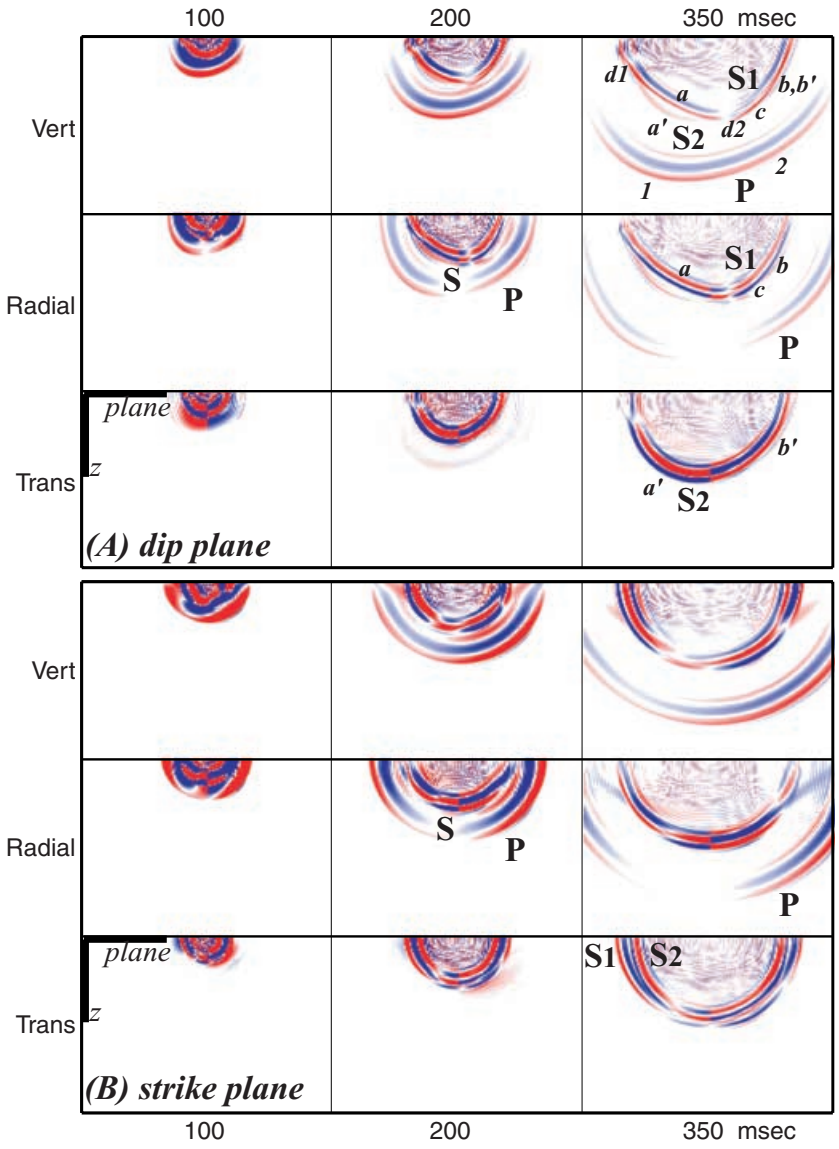

Figure 7. Cross-sections for the same cube as in Fig. 6 revealing wave propagation behaviour with depth. (a) A slice taken in dip direction (Fig. 1b). Foliation dips at 60° towards the left; the fast *P*-wave direction is the same. The radial component reveals two *S* waves that are split in one direction. The transverse component lacks a *P* wave. (b) The slice taken in the strike direction. *P*- and *S*-wave motions are more uniform in different directions within this plane. The *P* wave is faster in the horizontal direction owing to a stronger component of in-the-dipping-foliation plane. The *S* wave is not split vertically but is beginning to split in the pure horizontal direction.

and splitting along its elliptical wave front at 350 ms. We note that owing to 3-D propagation for these phases, the phase names *SV* and *SH* do not always indicate true particle directionality.

Vertical slices through the material cube also reveal downward propagation behaviour. Wave propagation in slices oriented in the true dip and strike directions (Fig. 1b) are shown in Fig. 7 for the same time steps as in Fig. 6. In exactly the true dip direction for this cube, propagation is 2-D involving only material dip with no influence from strike. In this dip plane, the *P* wave propagates elliptically with its elongation direction correlating with the material dip of 60° (Fig. 7a). The *S* wave splits when also propagating in the downdip direction; however, unlike in Fig. 6(a), the S2 phase is faster in this direction.

Fig. 7(b) illustrates wave propagation in a depth slice oriented in the strike direction. Material orientation and velocity behaviour are symmetric about the source point in the strike plane but have the added complexity that *P*- and *S*-wave particle motions are out of the strike plane along the dipping foliation planes. The horizontally propagating *S* wave (S1, S2) clearly splits in the strike direction.

REFRACTIONS/REFLECTIONS FROM THE TILTED ANISOTROPIC LAYER

The effect of material tilt on refraction/reflection propagation may be observed using a larger-scale earth model that has layers that will produce both refracted and reflected phases. In order to observe propagation effects owing to only material tilt, we generate a series of explosive sources

into a 150 km wide three-layer earth model wherein the top and bottom layers are isotropic and the middle anisotropic layer varies only by its internal tilt.

The top layer of this earth model has a V_P linear gradient between 4000 m s^{-1} at the surface and 5750 m s^{-1} at 10 km depth. The layer is isotropic and is assumed to be a Poisson material ($\sigma = 0.25$) in order to define its V_S gradient (2309–3320 m s^{-1}). The density is also a gradient between 2400 and 2700 kg m^{-3}. The isotropic bottom layer has a V_P gradient of 7500–8000 m s^{-1} from a depth of 20 km to the bottom of the model. This layer is also a Poisson material and its density is uniform at 3300 kg m^{-3}. The anisotropic middle layer at 10–20 km depth is composed of foliated schist with Haast velocities (Fig. 3). For this example the 2-D finite-difference implementation of eq. (1) is used to produce simulated seismograms. The earth model is 150 km wide and is padded to 150 km depth using a grid spacing of 35 m, an explosive pulse of 4–10 Hz and an internal time step of 0.002 s. The large vertical size is used to minimize bottom reflections of horizontally travelling refractions that can appear when using standard vertical-incidence reflection-absorbing boundary conditions. Each shot profile in Fig. 8 required 1.42 Gbytes of memory and 126.36 cumulative CPU hours of computer resources.

In Fig. 8 refraction shot profiles are shown using reduced traveltime ($v = 6.0$ km s^{-1}) for the cases when the middle layer tilt is 0° (no tilt), 90° (vertical), −45°, randomly oriented and coherently variable using an undulatory (antiform–synform) pattern. In the case where there is no tilt, distinct refracted and reflected phases from the different layers are observed (Fig. 8a). The direct phase through the top layer (P_t) shows the effect of the velocity gradient and merges into the refraction through the middle layer (P_m). The extra short branch in the triplication between P_t and P_m is caused by the jump in the horizontal velocity (from 5750 to 6468 m s^{-1}) even though the vertical velocity is the same across this interface (5750 m s^{-1}). P_m has responded to the horizontal velocity of the middle layer (6501 m s^{-1}) as does the reflection (P_mP) at wider source–receiver offsets (e.g. asymptotic traveltimes). The bottom layer refraction (P_b) emerges at a crossover distance beyond 100 km.

The P_m refraction phase can be seen in Figs 8(b)–(e) to respond to the different material orientations within the middle layer. In Fig. 8(b) the foliation is vertical so the refraction propagates horizontally using the 'slow' velocity normal to foliation. The P_m slope is positive in reduced traveltime because the horizontal velocity of 5750 m s^{-1} is less than the reduced velocity. In Fig. 8(c) the foliation dips at −45° and the P_m phase appears with an apparent velocity faster than in Fig. 8(b) but slower than the reduction velocity. This is in agreement with the V_{P45° value of 5881 m s^{-1} being marginally faster than that normal to foliation. In Fig. 8(d) the foliation dips are randomly oriented on a per node basis so that the overall range of dips is uniformly distributed between 0 and ±90°. The propagating waves encounter all velocities between the slow and fast Haast velocities. The material tilt is fully heterogeneous on such a fine scale that the middle layer behaves isotropically. P_m propagates at an average velocity of approximately 5960 m s^{-1}; the average velocity is not the velocity at the average dip (V_{P45°). Finally, since geological features do not usually have constant dip, a middle layer of smoothly variable dip is examined. In this case the tilt undulates sinusoidally between −45° to 45° to mimic a pair of 75 km wavelength antiforms and synforms (Fig. 8e). The refraction through this undulatory material behaves accordingly—the P_m arrival has a net intermediate apparent velocity but exhibits local undulations caused by its upward path encountering different foliation dips.

The P_mP reflection produced at the bottom of the middle layer also responds to the tilt of the anisotropic material. In all five cases in Fig. 8, this P_mP exhibits hyperbolic curvature that is asymptotic to the horizontal velocity (associated P_m refractions). In the case of the antiform/synforms (Fig. 8e), the undulating P_mP phase has a second branch at far offsets that could mistakenly be interpreted as a separate reflection from a deeper layer.

The P_b refraction propagates within the bottom layer in the same manner for all five cases and should exhibit the same apparent velocity. However, its appearance in the shot gathers is affected by delays introduced as P_b encounters the middle layer during its near-vertical downward or upward path. For case A in Fig. 8, the near-vertical direction is associated with the slow *P*-wave velocity direction, adding a delay to the P_b phase. This is in contrast to cases B–D where faster velocities are associated with the near-vertical direction, creating smaller delays. In the reduced traveltime displays in Fig. 8, these delays manifest themselves in the P_b crossover distance—a larger time delay increases the traveltime of P_b, making it emerge from the P_m at a later time and hence larger offset.

The most severe example of P_b time delay is exhibited by the antiform/synform middle layer (Fig. 8e). In this case, the undulation of the P_b arrival could be misinterpreted as being caused by lateral velocity variation in the bottom layer. However, the behaviour of P_mP would suggest that it is caused by lateral variations in the middle layer: if the P_b undulations were caused by the lower layer, the P_mP reflection might vary laterally in amplitude but would not undulate in traveltime.

LATERAL HETEROGENEITY OF TILT: ANISOTROPIC ANTIFORM

A 3-D antiformal structure is used for the final example of how material tilt affects seismic wave propagation. A source at depth will illuminate the structure with a range of ray path-material angles owing to both source-array geometry and material tilts associated with the antiform. We create an antiform model by arching the foliation of a uniform material described by Haast schist velocities and density. The antiform has dips ranging between ±64° in the *x*–*z* plane (Fig. 9). The earth block is constructed to be a cube of 30 km width with a node spacing of 100 m. A source is placed at depth so that only a one-way upward path through the antiform needs to be considered; a 1–5 Hz point source is located at (7.5, 8.0 km) in the (*x*, *z*) plane on the front face ($y = 0$). Propagation is calculated using a time interval of 0.005 s. An H-shaped surface array is located along the front and back edges (subarrays A and C, respectively) with a cross-bar subarray (B) connecting the two edges. 11 three-component stations are distributed every 3 km along each subarray. The cross-bar subarray is subparallel to but not located directly over the axis of the antiform. Rather, it is located at the up-dip projection of the foliation tilt that exists at the source location (57°). As a result, subarray B connects stations A7 and C7 (Fig. 9a). The horizontal *x*- and *y*-components in Fig. 9 are rotated into radial and transverse

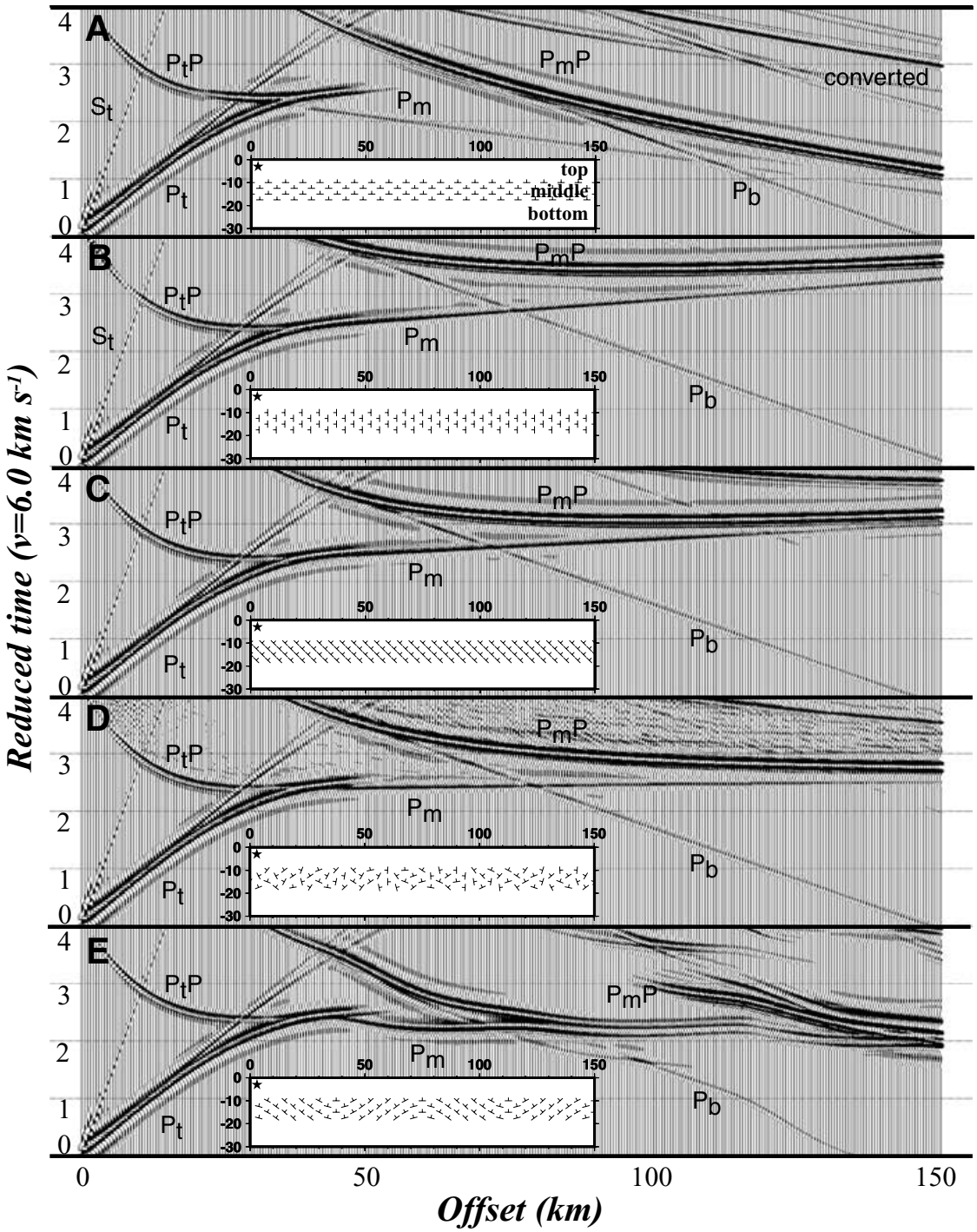

Figure 8. Effect of internal fabric tilt within a flat layer on refraction/reflection traveltimes. A three-layer model is used where the middle layer is uniformly anisotropic and has a tilted internal fabric. Top and bottom layers are isotropic with vertical velocity gradients; see the text for model values. Wide-angle refraction shots are simulated through this model; resulting shot profiles are displayed in reduced traveltime. P_t, P_m and P_b are the direct/refracted phases through the top, middle and bottom layers, respectively. Reflections originate from the base of the top (P_tP) and middle (P_mP) layers. (a) The middle layer fabric tilt is at 0° (subhorizontal). P_m travels in the 'fast' direction layer. (b) The fabric tilt at 90° (vertical). P_m travels at the 'slow' velocity. (c) The fabric tilt at −45°. Phases appear similar to the 90° case. (d) The fabric tilt is randomly oriented between 0° to ±90° on a per node basis. (e) The fabric tilt undulates between −45° to 45° with a wavelength of 75 km. P_m exhibits an averaged apparent velocity through the layer but undulates because of the antiform-synform tilt behaviour. P_mP and P_b also undulate; this latter undulation could mistakenly be attributed to lateral velocity heterogeneity within the bottom layer.

components relative to the surface location of the source. This simulation required 11.81 Gbytes of memory and 175.52 cumulative CPU hours.

As the seismic wave propagates through the antiform, its *P* and *S* waves can be observed to reach the surface and sweep across the surface arrays towards the back of the earth block. In Fig. 9(b) the *S* wave has reached the surface by 2.5 s. By 4.5 s the *P* wave has nearly reached

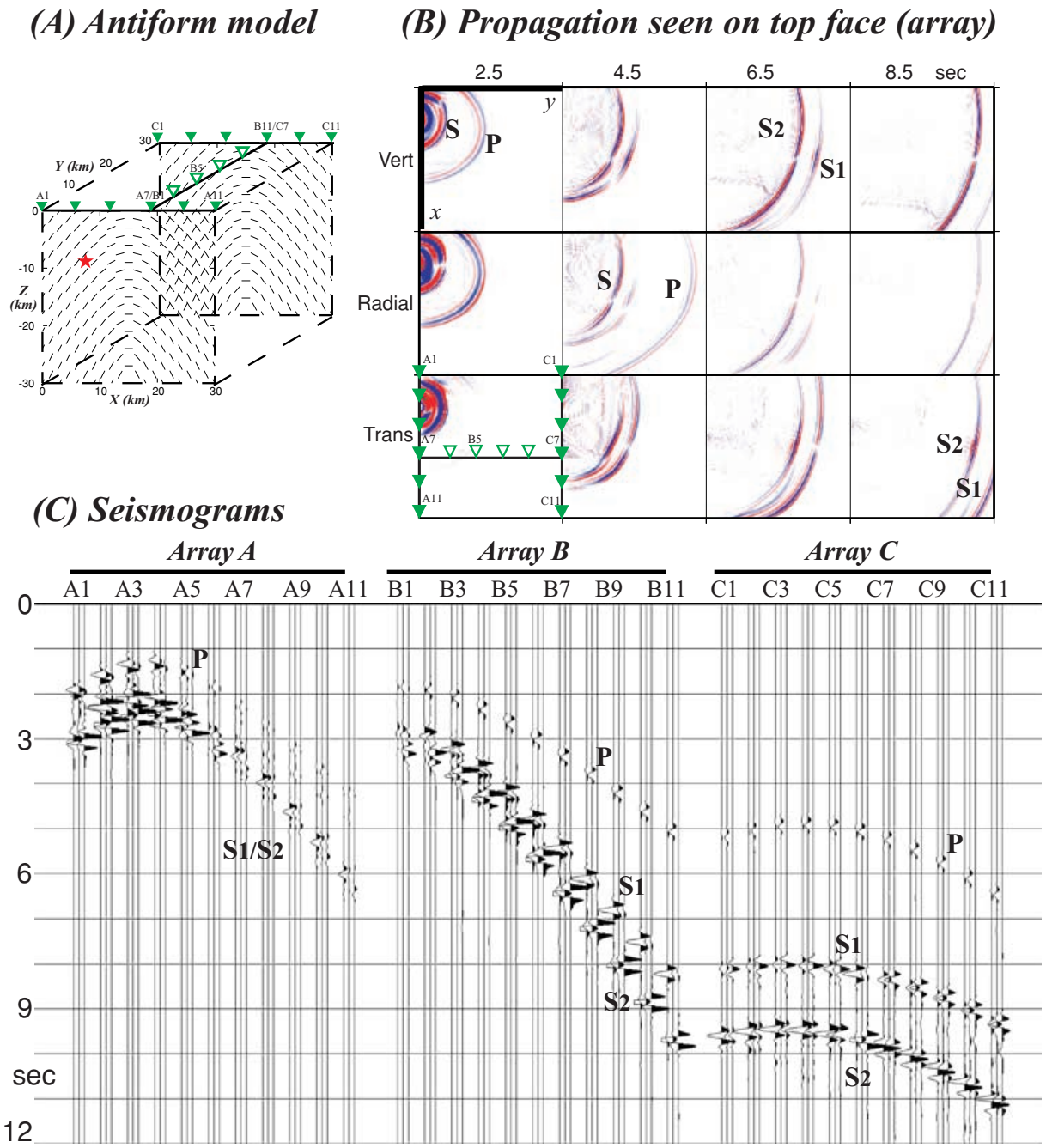

Figure 9. Wave propagation through a 3-D antiform. (a) Antiformal model where the anisotropic velocities are uniform and only the dip of the foliation has variation. Dimensions of block are 30 × 30 × 30 km at 100 m spacing. Arrays A–C are used to collect synthetic data from a source located at (7.5, 8.0 km) in the (x, z) plane on the front face ($y = 0$). An H-shaped array is defined on the top face. Subarray A is on top of the front face. Subarray B is located at the up-dip projection of the tilt found at the source point and is not located along the axis of the antiform. Subarray C is on top of the back face ($y = 30$ km). (b) Waveform propagation is along the top surface of the antiformal model. Red is positive seismic amplitude; blue is negative. Horizontal x- and y-components are rotated into radial and transverse components relative to the surface location of the source. At 2.5 s the S wave has propagated from depth to reach the surface and is now obliquely propagating in the y-direction. At 4.5 s the P wave has nearly reached the back of the model. The S wave begins to split. At 6.5 s the P wave is gone and the S wave has split and is more advanced in the y-direction than in the x-direction of propagation. (c) Seismograms collected at the A–B–C arrays. Each station has a triplet of seismograms representing the vertical, radial and transverse components. Partitioning of P- and S-wave energy among the three components vary across the arrays in agreement with the source–receiver geometry and the paths through the antiform.

the back of the block with an elongated wave front geometry. At 6.5–8.5 s the S wave reaching the surface has split (S1, S2) in the y-direction but has barely split in the pure x-direction.

For the seismograms collected by the A–C subarrays, partitioning of P- and S-wave energy into the vertical, radial and transverse components vary in agreement with source-to-receiver azimuth and ray path emergence inclination (Fig. 9c). Two effects related to the material arch are identified: the S wave does not have standard delay time relative to the P wave and the amount of shear wave splitting

increases, but not uniformly away from the source. These effects can be explained with an examination of ray path directions through the antiformal model. The *P* and *S* waves travel through different amounts of their respective 'slow' directions through the antiform. These differences make for non-uniform arrival time behaviour, although they are consistent with the 3-D geometry and orientations of the material anisotropy.

DISCUSSION

Calibration of synthetics to Christoffel equations

The *P*- and *S*-wave behaviour in the pure true dip direction as illustrated in Fig. 7(a) can be better understood with the aid of Christoffel equations (Hearmon 1961; Auld 1973). These equations provide *P*- and *S*-wave velocities at relative propagation angles, γ, oblique to material symmetry axes. In the case of a surface source located in uniformly dipping material (Figs 6 and 7), this relative propagation angle is $\gamma = \theta - \theta_{\text{dip}}$ measured between the downgoing wave direction, θ, and the material tilt, θ_{dip}. The Christoffel equations for hexagonal symmetry are thus:

$$\begin{aligned} q V_P^2(\gamma) &= (1/2\rho)\left(c_{11}\sin^2\gamma + c_{33}\cos^2\gamma + c_{44} + M^{1/2}\right) \\ q V_{SV}^2(\gamma) &= (1/2\rho)\left(c_{11}\sin^2\gamma + c_{33}\cos^2\gamma + c_{44} - M^{1/2}\right) \\ q V_{SH}^2(\gamma) &= (1/\rho)\left(c_{66}\sin^2\gamma + c_{44}\cos^2\gamma\right) \\ M &= \left[(c_{11} - c_{44})\sin^2\gamma - (c_{33} - c_{44})\cos^2\gamma\right]^2 + (c_{13} + c_{44})^2\sin^2 2\gamma, \end{aligned} \tag{4}$$

where stiffness coefficients are derived from petrophysical measurements

$$\begin{aligned} &c_{11} = \rho V_{P90^\circ}^2, \quad c_{33} = \rho V_{P0^\circ}^2 \\ &c_{44} = \rho V_{SV0^\circ}^2 \left(= \rho V_{SH0^\circ}^2 = \rho V_{SV90^\circ}^2\right) \\ &c_{12} = c_{11} - 2\rho V_{SH90^\circ}^2 \\ &c_{13} = -c_{44} + \left[\left(4\rho^2 V_{P45^\circ}^4\right) - \left(2\rho V_{P45^\circ}^2\right)(c_{11} + c_{33} + 2c_{44}) + (c_{11} + c_{44})(c_{33} + c_{44})\right]^{1/2} \\ &c_{66} = [c_{11} - c_{12}]/2 = \rho V_{SH90^\circ}^2 \end{aligned}$$

where $V_{P90^\circ} = P_{ab}$, $V_{P0^\circ} = P_c$, $V_{SH90^\circ} = S_{ab}$ and $V_{SV0^\circ} = S_c$ as illustrated in Fig. 3. The *P*- and *S*-wave velocities for all propagation angles within the true dip plane of the uniform tilt block of Figs 6 and 7 are shown in Fig. 10. The overall behaviour of the velocities is similar to that of an untilted hexagonal material (Fig. 1c) but is corrected for the 60° dip within the block. The velocities are labelled as quasi-waves since pure vibration directions are obtained only along the material axes. qV_P and qV_{SH} exhibit 2γ variation while qV_{SV} has 4γ variation.

This angular velocity variation explains the wave propagation behaviour seen in Fig. 7(a). The qV_{SH} and qV_{SV} curves in Fig. 10 are correlative with events S1 and S2 in Fig. 7(a), respectively. For a dip of 60°, a *P* wave propagating at −30° from vertical is parallel to the foliation plane and will encounter the fast V_P ('1' in Figs 7a and 10). From +30° to +90° qV_P is uniformly slow (2), accounting for the near-circular wave front curvature at 2 in Fig. 7(a). The qV_{SH} has its velocity maximum at −30°(*a*′) and its minimum at +60°(*b*′) to make its wave front, S2 in Fig. 7(a), elongate similar to the *P* wave. The qV_{SV} has one of its two velocity maxima at +15°(*c*) and minima at −30° and +60°(*a* and *b*, respectively) to form a wave front (S1) elongated in a direction different from the S2 wave. Maximum splitting of the two *S* waves occurs at −30° (*a*–*a*′ in Figs 7a and 10). In addition, the *S*-wave velocity curves cross at *d*1 and *d*2 in Fig. 10, forming singularity points where these waveforms meet in Fig. 7(a).

Fig. 7(b) illustrates wave propagation in a depth slice oriented in the strike direction. A similar analysis can be made to tie waveform behaviour in the strike direction with quasi-velocities as functions of the wave propagation direction. The Christoffel equations for the pure-dip

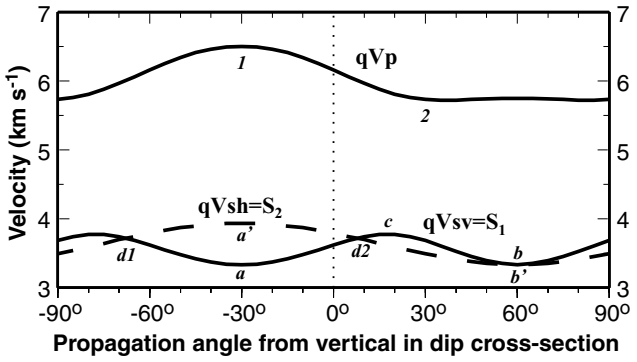

Figure 10. Velocity as a function of incidence propagation angle for the pure dip plane in Figs 1(b) and 7(a). Velocities calculated for hexagonal Haast schist velocities (at 600 MPa in Fig. 3) using Christoffel equations for a dip of −60° (cf. Fig. 1C, which has velocities in untilted schist). For a schist at −60° dip, the qV_P curve is shifted to align at −30° incidence angle; qV_{SV} and qV_{SH} are also shifted by −60°. Small italic letters and number denote important relationships between propagating phases that can be identified in Fig. 7(a). Maximum shear wave splitting occurs at *a*–*a*′ (parallel to the dipping foliation). Both *S* waves are identically slow at *b* (normal to foliation). Singularity points exist at *d*1 and *d*2 where no splitting occurs. The qV_{SV} (S1) is fastest at *c*, although the qV_{SH} (S2) is similar.

direction (eq. 4) can account for the foliation tilt by adjusting the relative propagation angle γ. However, these equations are not sufficient for calculation in the strike or any other plane because the material is tilted in 3-D and resulting *P* and *S* particle motions can be out of plane. A more complete set of Christoffel equations must be derived, which allow the propagation angle to be described as a vector quantity (azimuth and inclination, for example) or which uses a rotated stiffness tensor.

Computational impact

The employment of the full 21-element stiffness tensor in the elastic stress–strain equation (eq. 1) adds significantly to the computer memory requirements of the wave propagation code. We illustrate this point via comparison with the isotropic version of the same code, which uses only Lamé constants. The anisotropic 2-D example (Fig. 8) required 78 per cent additional memory and the 3-D examples (Figs 6, 7 and 9) required 2.2 times the memory that was needed to compute the same but isotropic cases. This increase in memory is directly attributed to the expanded stiffness tensors. The additional number of calculations in eq. (1) increased the 3-D anisotropic CPU runtime by 50 per cent. For the 2-D example, the anisotropic CPU usage increased by 10 per cent over its isotropic equivalent; this relatively small increase is explained by the 2-D form of eq. (1) having similar numbers of calculations when expressed using elastic stiffness elements or Lamé constants.

Geological relevance

The geological causes of crustal anisotropy include regional fractures and cracks, isotropic heterogeneity or layering and material composition and textural properties. In addition, shear or metamorphic foliations in fault zones or structural terranes serve as proxies for intracrustal deformation in a manner analogous to the lattice-preferred orientation of olivine produced by mantle shear. For real geological features within the crust, complex heterogeneous patterns exist in structure, composition, internal texture and dip. Material tilt as defined by rotated stiffness tensors can provide to these modelled features the characteristics of lateral variation, dipping boundaries and internal bedding or foliation that are not necessarily subparallel to contacts.

The above examples of synthetic anisotropic wave propagation suggest that the effects of material tilt on propagation arrival times and waveform shapes can be significant for seismic waves propagating within the crust. These synthetic examples are simple with uniform velocities so that only geometrical patterns of material tilt cause 2-D or 3-D effects of anisotropic behaviour. As is illustrated in Figs 7(a) and 10, the orientation of maximum shear wave splitting may no longer be in the horizontal or vertical directions owing to bulk material tilt. The anisotropic antiform in Fig. 9 indicates that 3-D structure relative to source–receiver geometries can produce systematic changes in observed shear wave splitting. Geological outcrops indicate that structures and material tilts change on many spatial scales. If these changes are very rapid relative to the path of the seismic wave, shear wave splitting effects may represent the average of the encountered material (Fig. 8d; Okaya & Christensen 2002) or may result in complex waveforms (Fig. 9).

While the examples presented here involve tilted hexagonal symmetries, the requirement of the full stiffness tensor for arbitrary tilt allows, prior to rotation, the use of orthorhombic or lower-ordered symmetries if they can be realistically described. The ability to produce anisotropic signatures within synthetic seismograms using realistic earth models provides a method by which interpretations may be calibrated with observed seismic data and will aid in the subsurface mapping of anisotropic terranes.

CONCLUSIONS

The effect of tilted anisotropic material on seismic wave propagation is determined by the relative angle between material orientation and ray path direction. For elastic wave propagation, materials can be characterized by elastic stiffness tensors of differing levels of symmetry that define the severity of anisotropy. Material tilt in any orientation may be produced by modification of its stiffness tensor that can be simplified to a matrix rotation when the reduced matrix notation is used. Since stiffness tensors have diagonal symmetry in reduced tensor form, nine elements are originally filled for hexagonal or orthorhombic symmetry based on five or nine independent coefficients, respectively. Tilt rotation will fill additional elements; rotation into an arbitrary orientation can fill all 21 reduced tensor elements. The numerical implementation of anisotropic wave propagation with tilted media thus requires a full tensor definition of stress–strain elasticity. Examples of synthetic seismograms indicate that tilted materials provide additional traveltime and waveform effects, which, for crustal propagation, can mistakenly be attributed to other regions of the crust or mantle.

ACKNOWLEDGMENTS

The authors thank Nik Christensen, Nicola Godfrey, Martha Savage and Mike Schoenberg for discussions that contributed to this study. The authors also thank Rob Graves, Rob Clayton, Leo Eisner, Stuart Henrys and Alan Levander for useful discussions on finite-difference methods and techniques. Reviews were provided by Chris Juhlin and an anonymous reviewer. Numerical computations were performed on the Geophysics multinode computing facility at the Department of Earth Sciences of the University of Southern California. This study was funded as part of an NSF–Continental Dynamics project (NSF EAR-9418530) and by NSF EAR-9980570.

Finally, DAO thanks co-author TVM (deceased 2002 February) for many years of sound wisdom on matters extending beyond seismology.

REFERENCES

Alkhalifah, T., 1995. Efficient synthetic-seismogram generation in transversely isotropic, inhomogeneous media, *Geophysics,* **60,** 1139–1150.

Auld, B.A., 1973. *Acoustic Fields and Waves in Solids,* Vol. I, p. 423, Wiley, New York.

Bond, W.L., 1976. *Crystal Technology,* p. 342, Wiley, New York.

Brocher, T. & Christensen, N., 1990. Seismic anisotropy due to preferred mineral alignment observed in shallow crustal rocks in southern Alaska, *Geology,* **18,** 737–740.

Carbonell, R. & Smithson, S.B., 1991. Large-scale anisotropy within the crust in the Basin and Range Province, *Geology,* **19,** 689–701.

Carcione, J., 1990. Wave propagation in anisotropic linear viscoelastic media, *J. Geophys. Int.,* **101,** 739–750.

Cerveny, V. & Firbas, P., 1984. Numerical modeling and inversion of travel times of seismic body waves in inhomogeneous anisotropic media, *Geophys. J. R. astr. Soc.,* **76,** 41–52.

Christensen, N.I., 1965. Compressional wave velocities in metamorphic rocks at pressures to 10 kilobars, *J. geophys. Res.,* **70,** 6147–6164.

Christensen, N.I., 1966. Shear wave velocities in metamorphic rocks at pressures to 10 kilobars, *J. geophys. Res.,* **70,** 3549–3556.

Christensen, N.I. & Crosson, R.S., 1968. Seismic anisotropy in the upper mantle, *Tectonophysics,* **6,** 93–107.

Christensen, N.I. & Ramananantoandro, R., 1971. Elastic moduli and anisotropy of dunite to 10 kilobars, *J. geophys. Res.,* **76,** 4003–4010.

Clayton, R.W. & Engquist, B., 1977. Absorbing boundary conditions for acoustic and elastic wave equations, *Bull. seism. Soc. Am.,* **67,** 1529–1540.

Cristescu, N., 1989. *Rock Rheology, Mechanics of Elastic and Inelastic Solids,* Vol. 7, p. 336, Kluwer, Dordrecht.

Daley, P.F. & Hron, F., 1979. *SH* waves in layered transversely isotropic media—an asymptotic expansion approach, *Bull. seism. Soc. Am.,* **69,** 689–711.

Davey, F.J. *et al.*, 1997. Preliminary results from a geophysical study across a modern, continent–continent collisional plate boundary—the Southern Alps, New Zealand, *Tectonophysics,* **288,** 221–235.

Faria, E.L. & Stoffa, P.L., 1994a. Finite-difference modeling in transversely isotropic media, *Geophysics,* **59,** 282–289.

Faria, E.L. & Stoffa, P.L., 1994b. Traveltime computation in transversely isotropic media, *Geophysics,* **59,** 272–281.

Fountain, D.M. & Christensen, N.I., 1989. Composition of the continental crust and upper mantle—a review, in *Geophysical Framework of the Continental United States,* Vol. 172, pp. 711–742, eds Pakiser, L.C. & Mooney, W.D., Geol. Soc. Am. Mem.

Frederiksen, A.W. & Bostock, M.G., 2000. Modelling teleseismic waves in dipping anisotropic structures, *Geophys. J. Int.,* **141,** 401–412.

Gajewski, D. & Pscencik, I., 1987. Computation of high-frequency seismic wavefields in 3-D laterally inhomogeneous anisotropic media, *Geophys. J. R. astr. Soc.,* **91,** 383–411.

Girardin, N. & Farra, V., 1998. Azimuthal anisotropy in the upper mantle from observations of *P*-to-*S* converted phases: application to southeast Australia, *Geophys. J. Int.,* **133,** 615–629.

Godfrey, N.J., Christensen, N.I. & Okaya, D.A., 2000. Anisotropy of schists: contributions of crustal anisotropy to active-source experiments and shear-wave splitting observations, *J. geophys. Res.,* **105,** 27 991–28 007.

Godfrey, N.J., Christensen, N.I. & Okaya, D.A., 2002. The effect of crustal anisotropy on reflector depth and velocity determination from wide-angle seismic data: a synthetic example based on South Island, New Zealand, *Tectonophysics,* **355,** 145–161.

Graves, R.W., 1996. Simulating seismic wave propagation in 3D elastic media using staggered-grid finite differences, *Bull. seism. Soc. Am.,* **86,** 1091–1106.

Grechka, V. & McMechan, G., 1996. 3-D two-point ray tracing for heterogeneous, weakly transversely isotropic media, *Geophysics,* **61,** 1883–1894.

Grechka, V. & McMechan, G., 1997. Analysis of reflection traveltimes in 3-D transversely isotropic heterogeneous media, *Geophysics,* **62,** 1884–1895.

Hearmon, R.F.S., 1961. *An Introduction to Applied Anisotropic Elasticity,* p. 136, Oxford University Press, London.

Helbig, K., 1993. Simultaneous observation of seismic waves of different polarization indicates subsurface anisotropy and might help to unravel its cause, *J. appl. Geophys.,* **30,** 1–24.

Hung, S.-H. & Forsyth, D., 1998. Modeling anisotropic wave propagation in oceanic inhomogeneous structures using the parallel multidomain pseudospectral method, *Geophys. J. Int.,* **133,** 726–740.

Igel, H., Mora, P. & Riollet, B., 1993. Anisotropic wave propagation through staggered finite-difference grids, *Can. J. Expl. Geophys.,* **29,** 53–77.

Jaeger, J.C. & Cook, N.G.W., 1976. *Fundamentals of Rock Mechanics,* p. 585, Wiley, New York.

Jones, K., Warner, M., Morgan, R., Morgan, J., Barton, P. & Price, C., 1996. Coincident normal-incidence and wide-angle reflections from the Moho: evidence for crustal seismic anisotropy, *Tectonophysics,* **264,** 205–217.

Juhlin, C., 1995. Finite-difference elastic wave propagation in 2D heterogeneous transversely isotropic media, *Geophys. Prospect.,* **45,** 843–858.

Keith, C. & Crampin, S., 1977. Seismic body waves in anisotropic media: synthetic seismograms, *Geophys. J. R. astr. Soc.,* **49,** 225–243.

Levander, A.R., 1988. Fourth-order finite-difference *P–SV* seismograms, *Geophysics,* **53,** 1425–1436.

Levin, V. & Park, J., 1997. *P–SH* conversions in a flat-layered medium with anisotropy of arbitrary orientation, *Geophys. J. Int.,* **131,** 253–266.

McNamara, D.E. & Owens, T., 1993. Azimuthal shear wave velocity anisotropy in the Basin and Range province using Moho P_s converted phases, *J. geophys. Res.,* **98,** 12 003–12 017.

Mensch, T. & Rasolofosaon, P., 1997. Elastic-wave velocities in anisotropic media of arbitrary symmetry—generalization of Thomsen's parameters , δ, and γ, *Geophys. J. Int.,* **128,** 43–64.

Nye, J.F., 1985. *Physical Properties of Crystals,* p. 329, Oxford University Press, London.

Okaya, D.A. & Christensen, N.I., 2002. Anisotropic effects of non-axial seismic wave propagation in foliated crustal rocks, *Geophys. Res. Lett.,* **10,** 1029/2001GL014 285.

Okaya, D., Christensen, N., Stanley, D. & Stern, T., 1995. Crustal anisotropy in the vicinity of the Alpine Fault, South Island, New Zealand, *New Zealand J. Geol. Geophys.,* **38,** 579–583.

Payton, R.G., 1983. *Elastic Wave Propagation in Transversely Isotropic Media,* Nijhoff, Dordrecht.

Rabbel, W. & Luschen, E., 1996. Shear wave anisotropy of laminated lower crust at the Urach geothermal anomaly, *Tectonophysics,* **264,** 219–233.

Russo, R.M. & Silver, P.G., 1994. Trench-parallel flow beneath the Nazca Plate from seismic anisotropy, *Science,* **263,** 1105–1111.

Sands, D.E., 1982. *Vectors and Tensors in Crystallography,* p. 228, Addison-Wesley, Reading, MA.

Savage, M., 1998. Lower crustal anisotropy or dipping boundaries? Effects on receiver functions, *J. geophys. Res.,* **103,** 15 069–15 087.

Savage, M., 1999. Seismic anisotropy and mantle deformation: what have we learned from shear wave splitting?, *Rev. Geophys.,* **37,** 65–106.

Savage, M., Silver, P. & Meyer, R., 1990. Observations of teleseismic shear-wave splitting in the Basin and Range from portable and permanent stations, *Geophys. Res. Lett.,* **17,** 21–24.

Silver, P.G. & Chan, W.W., 1991. Shear-wave splitting and continental mantle deformation, *J. geophys. Res.,* **96,** 16 429–16 454.

Tessmer, E., 1995. 3-D seismic modelling of general material anisotropy in the presence of the free surface by a Chebyshev spectral method, *Geophys. J. Int.,* **121,** 557–575.

Thomsen, L, 1986. Weak elastic anisotropy, *Geophysics,* **51,** 1954–1966.

Tsingas, C., Vafidis, A. & Kanasewich, E., 1990. Elastic wave propagation in transversely isotropic media using finite differences, *Geophys. Prospect.,* **38,** 933–949.

Virieux, J., 1986. *P–SV* wave propagation in heterogeneous media: velocity–stress finite-difference method, *Geophysics,* **51,** 889–901.

Zhu, J. & Dorman, J., 2000. Two-dimensional, three-component wave propagation in a transversely isotropic medium with arbitrary-orientation-finite-element modeling, *Geophysics,* **65,** 934–942.

APPENDIX A: DIRECTIONAL COSINES FOR A TILTED FOLIATION

The orientation of a tilted foliation can be expressed as the directional cosines between the symmetry axes of the bulk material and the geographical coordinate frame. These directional cosines may be obtained from the position of the material symmetry axes, *a–b–c*, using geological measurements of foliation plane strike and dip and lineation trend and plunge relative to *x–y–z* as shown in Fig. A1.

The material axes are oriented as follows. The *a*-axis is aligned with the lineation vector.

$$\mathbf{a} = \{a_x \quad a_y \quad a_z\} = \mathbf{L}. \tag{A1a}$$

The *c*-axis is normal to the foliation and hence can be described by the cross product of the strike and dip vectors:

$$\mathbf{c} = \{c_x \quad c_y \quad c_z\} = \mathbf{D} \times \mathbf{S}. \tag{A1b}$$

The cross product of **c** into **a** yields **b**:

$$\mathbf{b} = \{b_x \quad b_y \quad b_z\} = \mathbf{c} \times \mathbf{a} \tag{A1c}$$

With no rotation or tilt the *a–b–c* axes are aligned with *x–y–z*, respectively. The strike, dip and lineation vectors are obtained from field measurements strike, s_f, dip, d_f, trend, t_f, and plunge, p_f. These field measurements, which are commonly measured as azimuth clockwise from due north or dip from the horizontal, are converted to angles based on the unit sphere (azimuth counter-clockwise from *x* (east) and dip/plunge from the vertical (inclination): $s = 90^\circ - s_f$, $t = 90^\circ - t_f$, $d = 90^\circ + d_f$ and $p = 90^\circ + p_f$. The measurement vectors are:

$$\begin{aligned}
&\mathbf{S} = \{s_x \quad s_y 0\} = \{\cos s, \sin s, 0\} \\
&\mathbf{D} = \{d_x \quad d_y \quad d_z\} = \{\cos(s - \pi/2)\sin d, \sin(s - \pi/2)\sin d, \cos d\} \\
&\mathbf{L} = \{l_x \quad l_y \quad l_z\} = \{\cos t \sin p, \sin t \sin p, \cos p\},
\end{aligned} \tag{A2}$$

where the horizontal component of dip is perpendicular to the strike in accordance with the right-hand strike/dip rule (factor of $-\pi/2$). Substitution of the measurement vectors and trigonometric identifies into eq. (A1) yield:

$$\begin{aligned}
\mathbf{a} &= \{\cos t \sin p, \quad \sin t \sin p, \quad \cos p\} \\
\mathbf{c} &= \{d_y s_z - d_z s_y, \quad d_z s_x - d_x s_z, \quad s_x d_y - s_y d_x\} \\
&= \{-\sin s \cos d, \quad \cos s \cos d, \quad \sin d\},
\end{aligned} \tag{A3}$$

then

$$\begin{aligned}
\mathbf{b} &= \{c_y a_z - c_z a_y, c_z a_x - c_x a_z, c_x a_y - c_y a_x\} \\
&= \{\cos s \cos d \cos p - \sin d \sin t \sin p, \quad \sin s \cos d \cos p + \sin d \cos t \sin p, \quad -\cos d \sin p(\sin s \sin t + \cos s \cos t)\}.
\end{aligned}$$

The components of **a**, **b**, **c** are the directional cosines relating symmetry axes *a–b–c* to *x–y–z* as required within the Bond transformation matrix of Fig. 4.

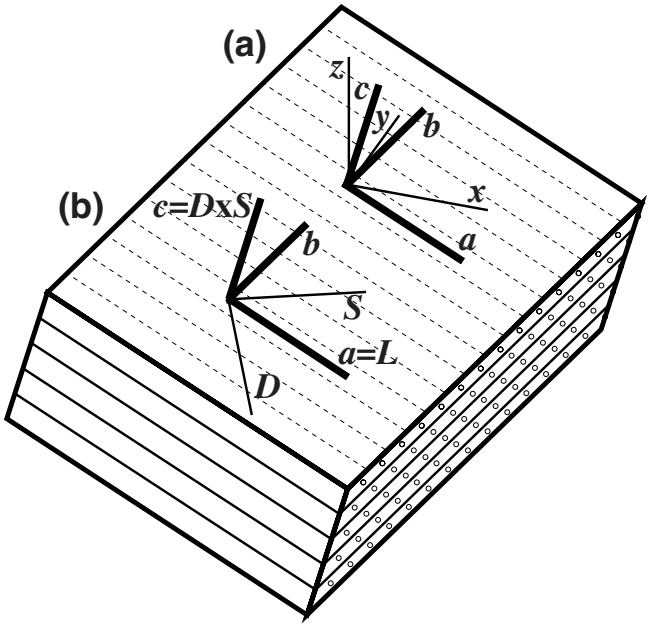

Figure A1. Coordinate axes for orthorhombic foliated dipping block. (a) *x–y–z* is geographical coordinate axes; *a–b–c* is material axes. (b) **S**–**D** are strike and dip of tilted foliation. **L** is lineation vector (plunge and trend). *a–b–c* can be derived from strike, dip and lineation. Hexagonal foliation has $a = b$ and no lineation.

No lineation exists for a hexagonal symmetry. Material tilt is defined solely by strike and dip of the foliation. Since behaviour within the planes of foliation are uniform for this symmetry, we may define the tilted *a*–*b*–*c* axes as follows. The tilted *a*-axis can be aligned with the dip vector and the *b*-axis with the strike vector:

$$\mathbf{a} = \{a_x \quad a_y \quad a_z\} = \mathbf{D} \tag{A4a}$$

$$\mathbf{b} = \{b_x \quad b_y \quad b_z\} = \mathbf{S}. \tag{A4b}$$

a and **b** are orthogonal and within the plane of foliation caused by the definition of strike and dip. The tilted *c*-axis is normal to the foliation and hence is the cross product of the strike and dip vectors:

$$\mathbf{c} = \{c_x \quad c_y \quad c_z\} = \mathbf{D} \times \mathbf{S}. \tag{A4c}$$

Using eq. (A2) and trigonometric identities, the directional cosines for hexagonal symmetry reduce to:

$$\begin{aligned} \mathbf{a} &= \{\sin s \sin d, \quad -\cos s \sin d, \cos d\} \\ \mathbf{b} &= \{\cos s, \quad \sin s, \quad 0\} \\ \mathbf{c} &= \{-\sin s \cos d, \cos s \cos d, \sin d\}. \end{aligned} \tag{A5}$$